Macromolecular Bioscience
www.mbs-journal.de

Synthesis and Incorporation of Quaternary Ammonium Silane Antimicrobial into Self-Crosslinked Type I Collagen Scaffold: A Hybrid Formulation for 3D Printing

Ranjeet Ajit Bapat, Senthil Kumar Muthusamy, Preena Sidhu, Kit-Kay Mak, Abhishek Parolia, Mallikarjuna Rao Pichika, Liang Lin Seow, Cao Tong, and Umer Daood**

Novel 3D-biomaterial scaffold is constructed having a combination of a new quaternary ammonium silane (k21) antimicrobial impregnated in 3D collagen printed scaffolds cross linked with Riboflavin in presence of d-alpha-tocopheryl poly(ethyleneglycol)-1000-succinate. Groups of "0.1% and 0.2% k21", and "0.1% and 0.2% Chlorhexidine (CHX)" are prepared. k21/CHX with neutralized collagen is printed with BioX. Riboflavin is photo-activated and examined using epifluorescence for Aggregatibacter actinomycetemcomitans (7-days). Collagen is examined using TEM and measured for porosity, and shape-fitting. Raman and tandem mass/solid-state are performed with molecular-docking and circular-dichroism. X-ray diffractions, rheological tests, contact angle, and ninhydrin assay are conducted. k21 samples demonstrated collagen aggregates while 0.1% CHX and 0.2% CHX showed irregularities. Porosity of control and "0.1% and 0.2% k21" scaffolds show no differences. Low contact angle, improved elastic-modulus, rigidity, and smaller strain in k21 groups are seen. Bacteria are reduced and strong organic intensities are seen in k21 scaffolds. Simulation shows hydrophobicity/electrostatic interaction. Crosslinking is observed in 0.2% CHX/79% and 0.2% k21/80%. Circular dichroism for k21 are suggestive of triple helix. XRD patterns appear at $d = 5.97, 3.03, 2.78, 2.1,$ and 2.90 A°. 3D-printing of collagen impregnated with quaternary ammonium silane produces a promising scaffold with antimicrobial potency and structural stability.

1. Introduction

The periodontium consists of an integrated, supporting, and functional unit of multiple tissues including but not limited to periodontal ligamentum, cementum, and alveolar bone.[1] Periodontitis is an inflammatory condition affecting periodontal tissues with horizontal or vertical bone defects leading to tooth exfoliation are the true endpoints of this disease.[2] The ultimate aim of periodontal therapy is to regenerate the lost bone with guided tissue regeneration (GTR) methods to achieve true periodontal regeneration.[3–5] Thus, it provides space maintenance and preserves the blood clot during the process of regeneration.[6] Resorbable membranes have been widely used to achieve periodontal regeneration, of these, collagen is the most widely used protein in membrane development.[7] With the proper mechanical and chemical stimuli, stem cells seeded on collagen scaffolds have the potential to differentiate down a myriad of cell lineages and become nearly any tissue in the human body. However, a prolonged periodontal condition may deteriorate the outcome of GTR by downgrading the healing capacity of periodontal cells, denaturalizing the extracellular matrix and inhibiting host immune response.[8] Collagen protein is an integral component of connective tissues having weak immunogenicity, augments tissue thickness and induces hemostasis during wound healing.[9–11] Studies have shown that use of collagen membranes with or without bone graft materials improves periodontal regeneration of intrabony defects.[12,13] These collagen membranes with or without bone

R. A. Bapat, P. Sidhu, A. Parolia, L. L. Seow, U. Daood
Division of Restorative Dentistry
School of Dentistry
International Medical University Kuala Lumpur
126, Jalan Jalil Perkasa 19, Bukit Jalil, 57000 Bukit Jalil, Wilayah Persekutuan, Kuala Lumpur, Malaysia
E-mail: umerdaood@imu.edu.my

S. K. Muthusamy, C. Tong
Oral Sciences
Faculty of Dentistry
National University of Singapore
21 Lower Kent Ridge Rd, Singapore 119077, Singapore
E-mail: dencaot@nus.edu.sg

K.-K. Mak, M. R. Pichika
School of Pharmacy
International Medical University Kuala Lumpur
126, Jalan Jalil Perkasa 19, Bukit Jalil, 57000 Bukit Jalil, Wilayah Persekutuan, Kuala Lumpur, Malaysia

The ORCID identification number(s) for the author(s) of this article can be found under https://doi.org/10.1002/mabi.202100326

DOI: 10.1002/mabi.202100326

graft have enhanced clinical attachment levels compared to open flap debridement.[14] 3D augmentation of these osseous defects will be the key aim of any regenerative procedure to obtain true regeneration. Tissue engineering can generate 3D tissue-like structures for biological studies, drug screening, and clinical applications such as implants.[15] 3D printing is a manufacturing process in which once a layer of the object is made, another layer is built upon that layer repeatedly, until the object has been produced in its entirety.[16] Due to its superior speed, 3D printing is often referred to as "rapid prototyping" as it is a popular choice to create product prototypes. Since collagen is the most abundant structural protein in mammalian tissues, it is an excellent choice to be utilized as the primary component of such versatile scaffolds[17] resulting in manufacturing of 3D collagen membranes to cover the osseous defects as per its configurations, that will help in selective bone formation by the osteoblast in 3-walled osseous defects.[18]

In this original research, a novel agent Quaternary ammonium silane (QAS; KHG FiteBac Technology, Marietta, GA, USA) was used as an antibacterial agent impregnated with collagen scaffold. QAS/k21 possesses functional end –OH group that can be altered to initiate the –OH groups.[19–22] The antibacterial action is due to its –C18H37 lipophilic alkyl chain that helps to penetrate the bacterial cell wall leading to autolysis[23] via contact killing.[24] The k21 molecule also elicits anti matrix metalloproteinase action that prevents further destruction of host tissues along with its broad-spectrum antibacterial activity with very low cytotoxicity.[25] The sol–gel process used for the design of silica-based materials undergo a strong hydrolysis process in the presence of water with the release of alcohol molecules in the presence of silanol Si–OH groups. The condensation reaction has a direct consequence on the particle growth (sol formation) and aggregation (gel formation), depending on the kind of pH applied, as more alkaline conditions form porous gels with dense networks[26] of vitreous silica that are thermodynamically stable.[27] leading to antimicrobial activities.[28] The experimental scaffold is hypothesized to provide a long-lasting antimicrobial efficacy basically because of quaternary ammonium molecules and its covalent attachment in the presence of the silanol groups.

Cross linking of collagen scaffold improves the mechanical characteristics and decreases the in vivo resorption of collagen.[29,30,31,32] Use of water-soluble RF and vitamin B12 added to collagen forms oxygen radicals by leading to cross-linking via photo-oxidation. This increases resistance to enzymatic degradation and enhancing of mechanical properties of these collagen matrices. Due to the presence of chemical permeation, enhancers like VE-TPGS, a non-ionic surfactant, RF uptake toward collagen is improved. VE-TPGS acts as RF transporter via various biological barriers. It has a protective function against reactive oxygen species formed during RF photoactivation.[33,34] Although there are several permeable enhancers investigated[35–37] with unclear permeation mechanisms, RF uptake is known to increase in the presence of these enhancers improving collagen crosslinking.[38]

Here, we describe the in vitro characterization of a new class of biomaterial combination to evaluate the antimicrobial effect in 3D collagen printed membranes cross linked with RF in presence of VE-TPGS as a potential scaffold. Thus, this novel 3D collagen scaffolds impregnated with novel QAS antibacterial biomaterial, cross-linked with VE-TPGS will provide a unique stable structure in bone formation for osseous defects around teeth and implant. This study therefore considered inclusion of architectural structures into potential mineralized collagen scaffolds to provide significant mechanical and biological advantage for regenerative medicine applications. The hypothesis tested was that a new class of biomaterial combination to evaluate the antimicrobial effect of QAS/k21 impregnated 3D collagen printed membranes cross linked with RF will not produce a stable structure; also, bacterial population owing to the effect of k21 modified scaffolds displays no effect, in relevance to single species biofilms.

2. Experimental Section

2.1. Experimental Design/Scaffold Fabrication

2.1.1. k21 Solutions

QAS (CaC2 enriched; ethanol-based solution form) was supplied by KHG fiteBac Technology, Marietta, GA, USA. The SiQAC molecule had been substituted with 3-(triethoxysilyl)-propyldimethyloctadecyl ammonium chloride (i.e., the ethoxy version of SiQAC, abbreviated as Et-SiQAC) and coupled with tetraethoxysilane by sol–gel synthesis (**Figure 1**). This resulted in a fully hydrolyzed ethanol soluble QAS molecule which was partially condensed S (1-octadecanaminium, N,N′-[[3,3-bis[[[3-(dimethyloctadecylammonio) propyl] dihydroxysilyl] oxy]-1,1,5,5,-tetrahydroxyl-1,5-trisiloxanediyl]di-3,1-propanediyl] bis[N, N-dimethyl] chloride (1:4); CAS number 1566577-36-3; codenamed K21). The yellow partially condensed k21 solid was mixed in absolute ethanol to produce solutions containing 0.1% and 0.2% k21 to be used in the experimental study (**Figure 2**).

2.1.2. Preparation of Collagen and Antimicrobial Mixture

Prior to and during the experiment, all components were kept on ice to maintain temperature (4 °C). To prepare the hydrogel, 1 part of 10× PBS (Vivantis) was mixed with 8 parts of collagen solution (Bovine, 6 mg mL^{-1} Nutragen, Advanced Biomatrix, Catalog No: 5010). Sterile 1 N sodium hydroxide (NaOH, Merck) was added to this mixture and was adjusted to pH 7. Antimicrobial solutions of k21 (KHG fiteBac Technology, Marietta, GA, USA) and CHX (CHX, Millipore Sigma, St. Louis, MO, USA) were mixed separately with neutralized collagen to achieve a final concentration of i) Conc 1 – 0.1% (1:19—1 part antimicrobial solution with 19 parts of neutralized collagen), ii) Conc 2 – 0.2% (1:9 – 1 part antimicrobial solution with 19 parts of neutralized collagen), iii) Conc 3 – (0) with no concentration). pH of the final collagen and antimicrobial mixture was tested to be neutral.

2.1.3. 3D Printing of Collagen Membrane

Without delay, the blended bioink was loaded into the cartridge specially designed to use with 3D bioprinter and maintained at 2–10 °C to prevent gelation. 3D collagen membranes were printed with BioX bioprinter (CELLINK) under pneumatic pressure (4 kPa) with optimal design and printing parameters (speed

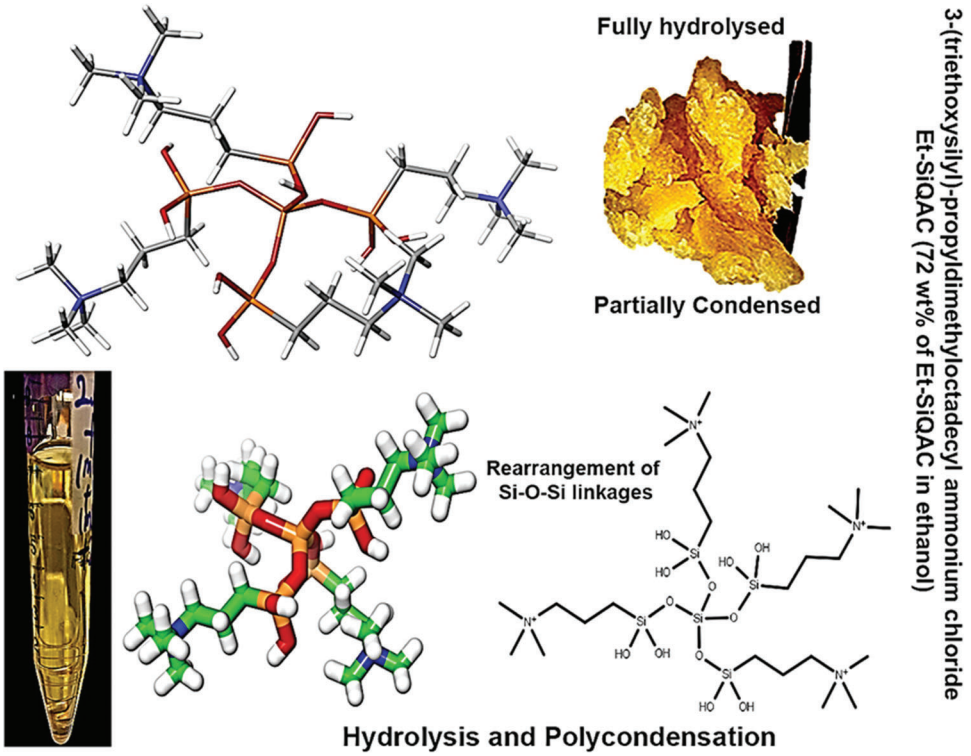

Figure 1. Proposed chemical formula of the quaternary ammonium molecule k21 based on organosilicon quaternary ammonium, 3-(trimethoxysilyl)-propyldimethy-octadecyl ammonium containing a long lipophilic C18 alkyl chain arm that has the ability to penetrate membranes causing cell death by direct contact and leaching of intracellular components. The compound is fully hydrolyzed, partially condensed QAS (1-octadecanaminium, N,N′-[[3,3-bis[[[3-(dimethyloctadecylammonio) propyl]dihydroxysilyl] oxy]-1,1,5,5,-tetrahydroxyl-1,5-trisiloxanediyl]di-3,1-propanediyl] bis[N, N-dimethyl] chloride (1:4); CAS number 1566577-36-3; codenamed K21 with central silicon atoms).

– 10 mm s^{-1}, nozzle diameter – 0.4 mm). 3D designing was done with the help of Slic3r software (GNU Affero, Slic3r) to generate the desired shape, size, thickness, and layer profile (pattern and infill density) of the printed collagen membrane.[39] The 3D printed membrane was incubated at 37 °C (30 to 60 min) for complete gelation. Further, printed membranes were stored at 4 °C in 1× PBS containing respective antimicrobial concentration to prevent shrinkage and dilution of the antimicrobial content.

2.1.4. Crosslinking Procedure

Riboflavin-5-phosphate (Sigma-Aldrich) was dissolved in distilled water to a concentration of 0.125% and stored in light proof test tubes to avoid spontaneous free radical production. Next, VE-TPGS at 50% concentration was added directly to the RF-solution, at RF/VE-TPGS (w/w) to obtain final ratios of 0.125/0.50 (RF/VE-TPGS0.50).[33] After centrifuging at 8000 rpm for 4 min to remove any suspended solids, the supernatant was filtered through 0.45 µm nylon filters (Lida, Kenosha, USA).

Formulations were than painted by one-application (10 µL) using a micro-brush for 60 s, left undisturbed for another 60 s, air-dried for 5 s, and finally photo-activated with UVA (368 nm, output 7 mW cm^{-2}) by placing the UVA source 10 mm away from the scaffold surface having a spot size of ≈6 mm such that the entire scaffold was fully irradiated with a single UVA irradiation spot.[33]

2.1.5. Bacterial Inoculation

The *Aggregatibacter actinomycetemcomitans* strains (ATCC 29 522, Microbiologics, USA) were obtained in KWIK-STIK pellets containing a pure population of microorganisms. The swab heavily saturated with the hydrated material and microorganisms was transferred to the blood agar plates (Brucella Agar with 5% sheep blood, 0.005 g L^{-1} of hemin and 0.01 g L^{-1} of vitamin K1, Isolab, Malaysia). Primary inoculation was performed by rolling the swab over the agar plate. Streaking was done with a sterile loop to enable colony isolation. Immediately inverted primary culture plate(s) were inoculated anaerobic conditions (90% air, 10% CO2) at 37 °C for one week and then transferred to a 10.0 mL of tryptic soy broth (BD DifcoTM, NJ, USA). The cell suspension was altered to match the turbidity of 1.5×10^8 CFUs mL^{-1} (equal to 0.5 McFarland standards). The bacterial inoculum was transferred to the printed collagen scaffold specimens ($n = 3$) in 24 microtiters well plate using sterile 5.0 mL syringes (Terumo, Somerset, NJ, USA) with 30-gauge needles (Terumo, Somerset, NJ, USA) in a biosafety cabinet. Following this inoculation, specimens were incubated for one week at 37 °C. After one week, the samples were used for testing of viability of organisms.

The specimens were washed and fixed using 2.5% glutaraldehyde in a phosphate buffered saline (PBS) solution (1.7 mM KH_2PO_4, 5 mM Na_2HPO_4 with 0.15 M sodium chloride, pH 7.2) for 10 h at 4 °C. After washing with PBS, the specimens were

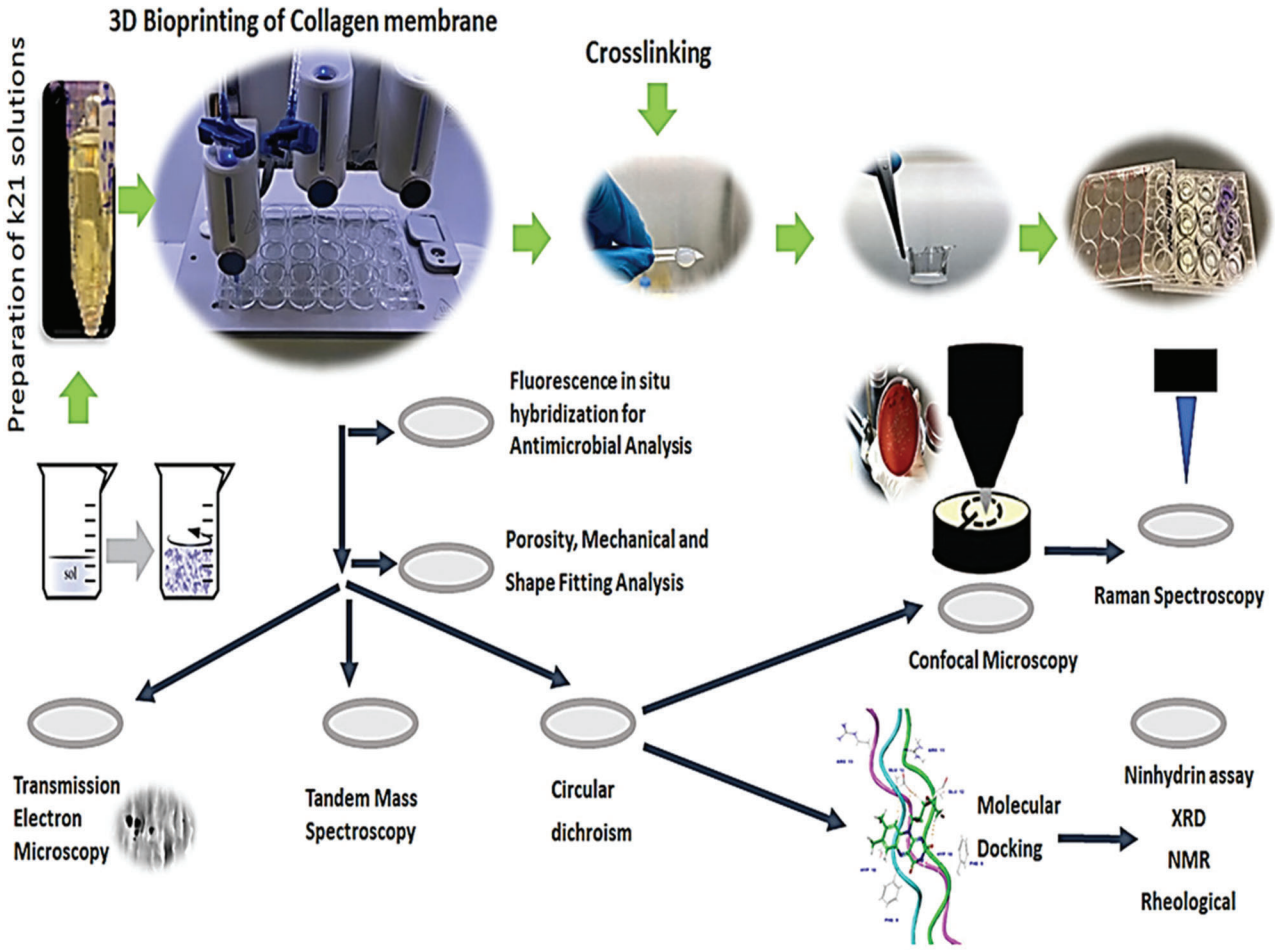

Figure 2. Fabrication of 3D scaffolds using customized 3D printer. A) 3D printer equipped with printing nozzle displaying schematic illustration of the printing process and photo-crosslinking process.

stored in a mixture of 50% ethanol and 50% PBS for ≈3 h at 4 °C. For the permeabilization of the bacterial cells, the scaffolds were further incubated using a solution of 7 mg mL^{-1} of lysozyme (hen egg white lysozyme, Fluka, Buchs, Switzerland, 105 000 U mg^{-1} in 0.1 M Tris–HCL, 5 mM EDTA, pH 7.2) for 12 min inside a humid incubator (37 °C). The specimens were than subjected to washing using double distilled water and dehydrated using ascending series of ethanol (75%, 80%, 95%, and 100%). Hybridization buffer (5 M NaCl, 1 M Tris–HCL (pH 8.0)) was mixed with 10% sodium dodecylsulfate and 25% formamide (v/v) in 24-well plates (Greiner Bio-One, Frickenhausen, Germany) which were covered with aluminum foils for 120 min at a temperature range between 44 to 46 °C. The specimens were than incubated in 600 µL wash buffer for 20 min using oligonucleotide probe ACT476 (59-ATC CAG CTA CCG TCA ACC39) (IBA) labeled with Atto550. All labeled specimens were examined using epifluorescence microscopy (Axioskop II, Zeiss, Oberkochen, Germany) at a magnification with scale bar of 50 µm with number of cells observed with microscopic ocular grids (area 0.0156 mm^2) of 10 per sample. The bacteria were calculated bacteria per cm^2 after 7 days ($n = 3$).

2.2. Transmission Electron Microscopy

The collagen fibril structure within the discs ($n = 3$) was performed using a JEM2100 (JEOL, Japan) Transmission Electron Microscope at 200 kV. The discs were fixed in 2.5% glutaraldehyde and dehydrated using ascending series of ethanol (70%, 80%, 90% and 100%) and embedded in epoxy resin. A collagen fibril was measured per transverse ultrathin section at the same magnification and calculated using Image-Pro Plus (IPP) 6.0 software (Media Cybernetics, Silver Spring, MD, USA). Around 200 fibers were randomly selected for counting.

2.3. Fluorescence In Situ Hybridization for Antimicrobial Analysis

The specimens were washed and fixed using 4% paraformaldehyde in a PBS solution (1.7 mM KH_2PO_4, 5 mM Na_2HPO_4 with 0.15 M sodium chloride, pH 7.2) for 10 h at 4 °C. After washing with PBS, the specimens were stored in 50% ethanol and 50% PBS mixture for ≈3 h at 4 °C. For the permeability of the bacterial cells, the scaffolds were further incubated using a solution of

7 mg mL^{-1} of lysozyme (hen egg white lysozyme, Fluka, Buchs, Switzerland, 105 000 U mg^{-1} in 0.1 M Tris–HCL, 5 mM EDTA, pH 7.2) for 12 min inside a humid incubator (37 °C). The specimens were than subjected to washing using double distilled water and dehydrated using ascending series of ethanol (75%, 80% 95%, and 100%). Hybridization buffer (5 M NaCl, 1 M Tris–HCL (pH 8.0)) was mixed with 10% sodium dodecylsulfate and 25% formamide (v/v) in 24-well plates (Greiner Bio-One, Frickenhausen, Germany) which were covered with aluminum foils for 120 min at a temperature range between 44 to 46 °C. The specimens were than incubated in 600 µL wash buffer for 20 min using oligonucleotide probe ACT476 (59-ATC CAG CTA CCG TCA ACC39) (IBA) labeled with Atto550. All labeled specimens were examined using fluorescence microscopy (Axioskop II, Zeiss, Oberkochen, Germany) at a magnification with scale bar of 50 µm with number of cells observed with microscopic ocular grids (area 0.0156 mm^2) of 10 per sample. The bacteria were calculated bacteria per cm^2 after 1 and 3 days. Stacks of fluorescent images of the biofilm were examined using the bioimageL software (v.2.0, Malmö, Sweden), which provides information on the structure of the biofilm, including green and red-stained bacteria volume on a 2D x–y section based on MATLAB-written color segmentation algorithms. For each group, the percentages of live and dead bacteria were calculated.

2.4. Porosity, Mechanical, and Shape Fitting Analysis

The scaffold specimens ($n = 3$) were weighed in a dry state and then immersed in 10 mL ethanol. After immersion, the specimens were weighed again, and porosity measured using the following equation:

$$Porosity = \frac{(W_w - W_d) \times 100\%}{\rho x \pi R^2 T} \quad (1)$$

W_w / weight of scaffold in wet
W_d / weight of scaffold in dry
ρ / solvent density
R / radius of scaffold
T / thickness of scaffold

The scaffolds were also tested under mechanical compression for the analysis of elastic modulus ($n = 3$) using Instron 5943 mechanical tester (Instron) with a 100 N load cell at a rate of 1 mm min^{-1}. The Matlab program was used to determine Young's modulus for a stress/strain curve of liner proportion. The scaffolds were also fitted inside a 5.5 mm Teflon diameter hole and pushed through with maximum force ($n = 8$) to determine stiffness and shape fitting stability.

A nanoindentation test was also performed at desired time points using a G200 Nano-indenter (Agilent 7 Technologies, Santa Clara, CA, USA) at a constant strain rate of 0.05 s^{-1} and a depth of 70 nm ($n = 5$). The hold-time was set at 5 s and enabled a load range of 300–400 µN. Ten indentations were done randomly on each specimen with a lateral spacing of 400 nm to confirm the elastic moduli readings achieved using the Instron machine. The reduced elastic-modulus (Er) and nano-hardness (H) were calculated.

2.5. Raman Spectroscopy Analysis Understanding Biochemical Structure

The Raman analysis ($n = 3$) was performed in a combined forward-viewing probe based automated system after choosing a region of interest created by dividing the specimen into quadrants using LabRam spectrometer (Horiba Jobin Yvon, Lille). The measurements were acquired in the same 900 Raman-point region on a ≈4 mm^2 divided sample. Prior to the measurement, a calibration of the Raman set driven scanning probe was performed (25 mW after the objective). Following the acquisition of the hyperspectral Raman image of the desired region, the signal was collected with the Raman laser equipped with 105 µm multimodal fiber connected to a 785 nm single-mode excitation laser (Fergy-Laser, Princeton Instruments). At a magnification of 1 onto the sample, the resultant spot size was nominal with an output power of 70 mW which was focused on a spot size of 100 µm and a spectral resolution of 5 cm^{-1}. The signal range was between 400 to 3200 cm^{-1} with an acquisition time of 20 s for each spectrum and 2 accumulations from 10 points which were randomly selected using a 100× objective (Olympus NA 0.8). The collected scattered light was grated using 950 g mm^{-1} disperses by means of couple charged detector. All Raman spectral spectra were baseline corrected and normalized by subtracting a 4th order polynomial fit. The mean centered principal components analysis was employed on control and experimental groups data in associated with different variables to explore the eventual spectral variabilities of all the data sets, but not included in the final analysis. Images were reconstructed by defining Raman shift regions of Amide I, II, III bands along with hydroxyproline, tyrosine, and tryptophan at β angles of polarization in the steps of $\Delta\beta = 15°$, from $\beta = 90°$ and $\beta = -90°$.

2.6. Proline and Hydroxyproline Analysis of Collagen via Tandem Mass Spectroscopy

The tandem mass spectroscopy of the printed scaffolds ($n = 3$) was performed directly. The specimens were placed directly inside a petri dish using a cyanoacrylate adhesive. The dish was attached to a metal support. The fragmentation of selected peptides was performed at a minimum 60 000 using MS and MS/MS scans. The method used was collision induced dissociation (CID) and Swiss Prot database with MASCOT search engine for annotation of MS/MS spectra. The data was interpreted (addition of 16 Da to the mass of proline residue) as a modified parameter in MASCOT search engine with each fragment ion analysis and proline oxidation for detection of Hyp PTM present in COLIIA1 peptide sequences.

2.7. Solid-State NMR Spectroscopy: 1

A Burker AVANCE III HD spectrometer (Larmor frequencies $\nu^{13}C = 125.783$ MHz) was used with a 3.2 mm MAS probe for recording of solid-state NMR. The ^{13} C CP/MAS NMR spectra were obtained with a spinning speed of 20 kHz. There was a repetition delay of 10 s as the ^{13} C CP/MAS NMR scans (2048) with a spinlock of 1 ms were recorded. The glycine shift of the ^{13} C

CP/MAS scale with a standard glycine (176.03 ppm to carbonyl signal) at 303 K. ($n = 3$).

2.8. Molecular Docking

To replicate the collagen fiber printing of the scaffold, and to structurally align the same domain in the crystal structure of collagen Type I (integrin $\alpha 2$ I-domain (PDB: 1DZI)) of the scaffold, the collagen Type I peptide was removed, and simulation performed using Schrodinger small-molecule drug discovery suite 2019-4. Crystal structures of collagen (PDB ID: 6A0C) were downloaded from the Research Collaboratory for Structural Bioinformatics Protein Data Bank (http://www.pdb.org; Wednesday 12:30 ET, 2021). The collagen structure determined was neutralized with ions with a minimum gap of 5 nm to avoid self-interactions and a strong force field. Around 20 replicas were introduced, and temperature was maintained between 300 and 400 K. The binding energy of the collagen complex with integrins was sampled with the 20 replicas created removing the bound Mg ion to confirm the binding. The center of masses of each triple helix created was bound with the $\alpha 2$ I-domain integrin depicting collagen crosslinking.

2.9. Circular Dichroism

Circular dichroism was conducted ($n = 3$) using Jasco 815 Circular Dichroism Spectropolarimeter (MIMOS laboratory, MY) in a nitrogen atmosphere within a UV range of 190–260 nm. The scan was carried out with 0.2 nm intervals and a path length of 1 mm with three scans getting averaged. Data was analyzed using milli degrees and converted to molar ellipticity (d mol^{-1}) which was plotted against the wavelength.

2.10. XRD

The presence of calcium chloride ($CaCl_2$) and the crystal structure of the collagen within the 3D scaffold was analyzed using a Bruker D8 Advance diffractometer (40 kV, 40 mA) for X-ray diffractometry with Cu K_α radiation n (Billerica, MA, USA). The scanning rate was set at 0.02° s^{-1} and 2θ with 10°–75° range. A pristine collagen sample from dentin (dentin powder) was by XRD as a control. Three 2 mm dentin discs were pulverized using a mortar pestle and placed in the silicon sample holder for the analysis.

The presence of $CaCl_2$ and the crystal structure of the collagen within the 3D scaffold, a Bruker D8 Advance diffractometer (40 kV, 40 mA) was used for X-ray diffractometry with Cu K_α radiation n (Billerica, MA, USA). The scanning rate was set at 0.02° s^{-1} and 2θ with 10°–75° range. A pristine collagen sample from dentin (dentin powder) was by XRD as a control. Three 2 mm dentin discs were pulverized using a mortar pestle and placed in the silicon sample holder for the analysis.

2.11. Rheological Tests

A stress rotational rheometer (TA instruments, Water, MIMOS laboratory, MY) was used for rheological analysis of the collagen formulation. The machine was equipped with a 20 mm diameter plate with Peltier plate for temperature control. A temperature of 4 °C was maintained for flow ramp tests to analyze the suspension viscosity for a shear rate of (0.01–1000 s^{-1}).

2.12. Contact Angle

The hydrophilicity of each scaffold ($n = 3$) was determined by the water contact angle (CA) analysis by placing the water (same amount) on each scaffold and measuring using CA meter instrument (KINO SL200B/K Series, USA).

2.13. Ninhydrin Assay

The number of free amino acids within the crosslinked scaffolds were evaluated using ninhydrin assay. The ninhydrin solution was prepared using 5 mL of ethanol per mg of collagen and mixed with 0.25 g of ninhydrin. The solution was added to the scaffolds placed in the well-plates and sealed using Parafilm. The plates were left for heating at 80 °C for 20 min. After heating, the plates were cooled and eluted with 50% isopropanol (1.25 mL isopropanol per 1 mL of ninhydrin solution). Ruhemann's purple dye (200/1) was added to a 96 well plate with the elution and the absorbance read at 570 nm using a using a SPECTRO star Nano plate reader (BMG LABTECH Ltd, Aylesbury, UK). After preparing the standard curve, the linear region of the absorbance was converted to specimen absorbances for the amine content. The degree of crosslinking was determined using the following formula:

$$\text{Degree of crosslinking (\%)} = \left(1 - \frac{\text{Amine Content in Sample}}{\text{Amine Content in non} - \text{crosslinked}} \times 100\%\right) \quad (2)$$

2.13.1. Statistical Analysis

Unless stated otherwise, the p value for all statistical tests were stated as $\alpha = 0.05$ as all datasets were subjected for homoscedasticity and normality. Where datasets were normally distributed, a one-way ANOVA was performed followed by Tukey post-hoc comparison. For datasets that are not passing the normality tests, Kruskall–Wallis non-parametric test and Mann–Whitney U post-hoc test were employed. The statistical values indicated are the statistical difference between the data point and the non-crosslinked values of specimens.

2.13.2. Ethics Approval

The ethical committee at International Medical University approved the study, protocol number IMU R5050/2020. All authors signed the consent forms.

3. Results

The morphology and microstructure of 3D-printed collagen scaffolds using customized 3D printer were analyzed using transmission electron microscopy. The collagen scaffold was designed

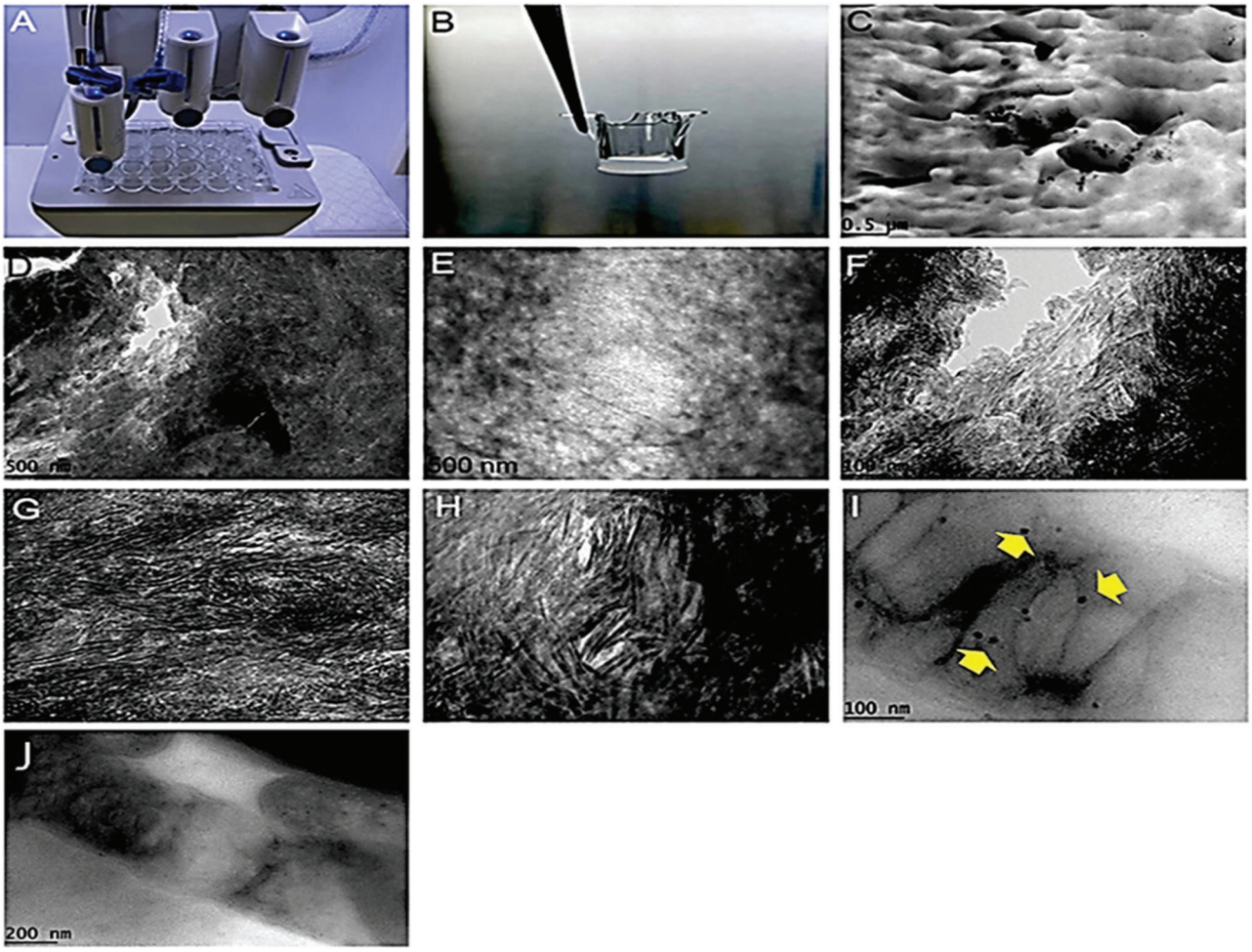

Figure 3. The morphology and microstructure of 3D-printed collagen scaffolds using customized 3D printer after transmission electron microscopy observation. A) Typical setup for printing B) high strength riboflavin/VE-TPGS crosslinked collagen scaffold; C) TEM image of a printed scaffold from the top surface (scale bar: 0.5 µm); D) TEM image of 0.1% CHX and E) 0.2% CHX showing collagen arrangement irregularities with no homogenization. The distribution appears skewed to smaller and thinner diameters as compared to F) 0.1% k21 and G,H) 0.2% k21 which are displaying the best measure of collagen fibrils. The fibers appear certainly of different lengths but with intact fibrils; I) high magnification of 0.2% k21 collagen fibril within the printed scaffold showing zones of k21 molecule attached into the collagen shaft (yellow arrows) as collagen fiber appears oriented too; J) single collagen fiber within control specimens. No deposition of interfibrillar k21 molecules was observed between the fibers

with alternating hydrophobic and hydrophilic amino acids that are self-assembled (**Figure 3**) to form a stable structure similar to that of a native extracellular matrix. The mean diameter for 0.2% k21 (Figure 3G,H) collagen scaffold was ≈300–350 nm demonstrating large aggregates with entangled formations when only k21 was used. TEM image of 0.1% CHX (Figure 3D) and 0.2% CHX (Figure 3E) showed collagen arrangement irregularities with no homogenization. The distribution appears skewed to smaller and thinner diameters as compared to (Figure 3F) 0.1% k21 and (Figure 3G,H) 0.2% k21 which are displaying the best measure of collagen fibrils. The fibers appear certainly of different lengths but with intact fibrils; high magnification of 0.2% k21 (Figure 3I) collagen fibril within the printed scaffold displayed zones of k21 molecule attached into the collagen shaft (yellow arrows) as a single collagen fiber can be identified with k21 infiltration. The enlarged view of single fibers in control specimens showed closely stacked single tubes with a homogenous separated distribution (**Figure 4**A,B). The collagen fibers after binding with k21 did not appear to be changed as indicated in (Figure 4A,B). No deposition of interfibrillar k21 molecules was observed between the fibers.

The porosity of the control (45 ± 5.5) and 0.1% k21 (50 ± 6.0) and 0.2% (40 ± 8.5) k21 scaffolds which showed no significant difference and indicated all the prepared scaffolds had a uniform porous micro-structure as compared to the CHX scaffold specimens (**Table 1**). There was significant improvement in the surface elastic modulus (E_{appr}) found after 24 h (crosslinking) in all k21 groups. The mean± standard of the apparent elastic modulus (E_{appr}) showed a significant reduction of 0.2% CHX scaffold as compared to other experimental groups. There was a significant difference of elastic moduli values between the control (4.8 ± 1.1)/k21 groups and the CHX modified groups marked by

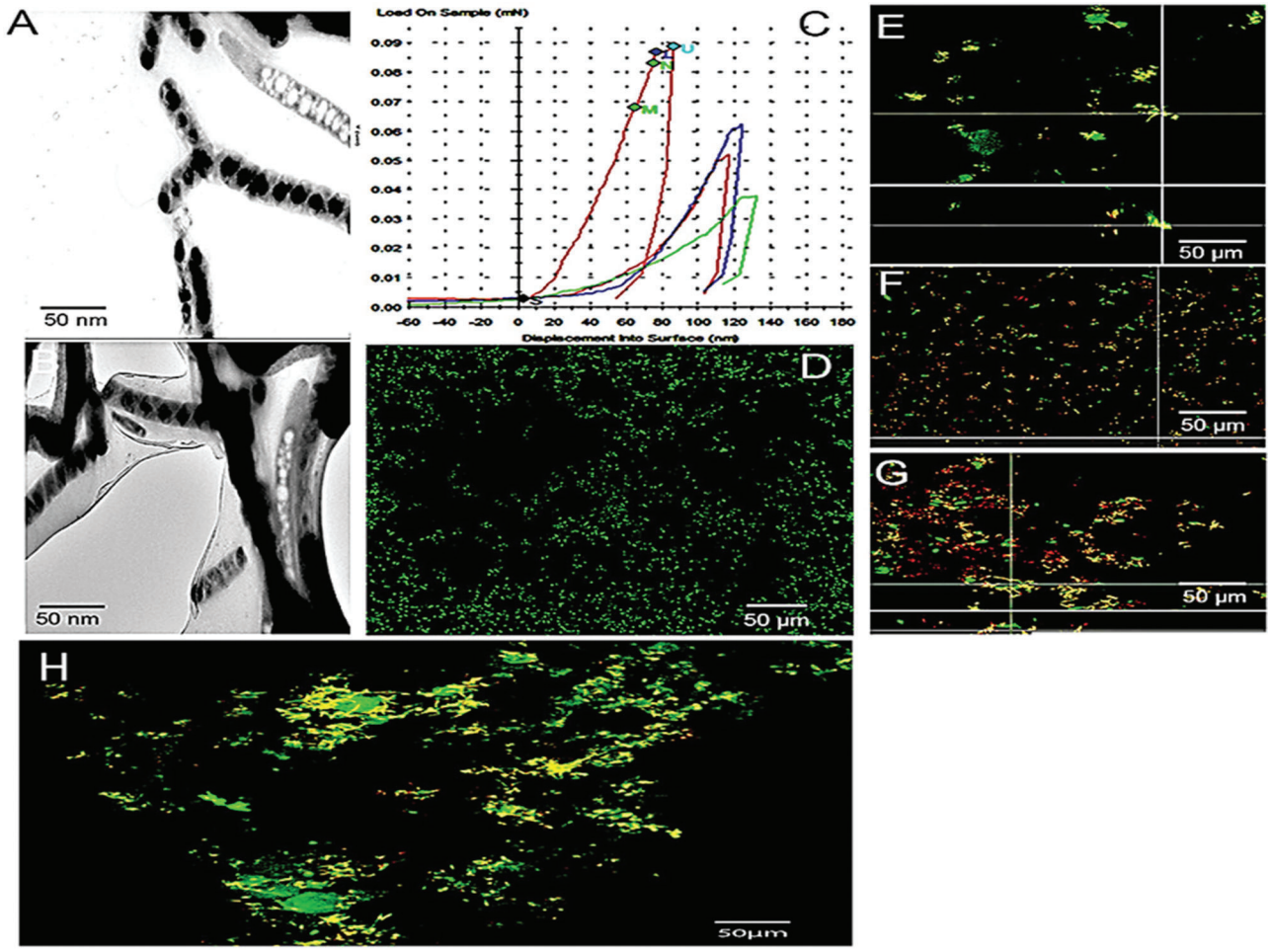

Figure 4. A,B) Microstructure of 3D-printed 0.2% k21 collagen scaffolds with collagen fibrils adsorbed with 0.2% k21. C) nanoindentation distance increase, with first indentation cycle. The visualization of bacteria with CLSM after FISH was performed with sectioning done at 0.97 µm and merged using Zeiss software. D) control; E) 0.1% k21; F) 0.2% CHX G) 0.2% k21; H) 0.1% CHX specimens.

Table 1. Summary of data obtained for mechanical property measurements of scaffold samples. Young's and ultimate strain of 3D-printed designs. ($p < 0.05$). Data expressed as mean ± standard deviation for all mechanical properties. E′ and tan (δ) values at 1 Hz ($E'_{1\,Hz}$ and tan $(\delta)_{1\,Hz}$) of hybrid scaffolds at different concentrations of k21 crosslinked with RF and live and dead percentages of bacteria. Values with different letters are significantly different ($p < 0.05$). Quantification of colony forming after desorption of bacteria from scaffold surfaces ($p < 0.001$).

Groups	Young's Modulus E_{appr}	Ultimate Strain [mm/mm]	Porosity [%]	CA	E′ 10^4 [Pa] 1 Hz σ	Tan [δ] 1 Hz	FISH [bacteria/cm^2]	Live Dead Bacterial Percentages	
								Live	Dead
Control	4.8 ± 1.1 A	0.27 ± 0.06	40 ± 5.5 A	7.4 ± 1.22°	1.3^E	0.9	890 000 cm^2	99.2 ± 11.1 A	0.8 ± 0.04 a
0.1% k21	5.2 ± 1.9 A	0.35 ± 0.09	50 ± 6.0 A	0°	0.9 ^{E}	0.12	140 000 cm^2	23.4 ± 4.7 B	76.6 ± 12.3 b
0.2% k21	4.1 ± 0.9 A	0.4 ± 0.07	40 ± 8.5 B	0°	0.8 ^{E}	0.17	60 000 cm^2	7.3 ± 2.2 C	92.7 ± 8.3 c
0.1% CHX	3.8 ± 0.8 B	0.29 ± 0.04	30 ± 7.5 C	2.1 ± 0.06°	0.9 ^{E}	0.11	190 000 cm^2	37.6 ± 5.9 D	62.4 ± 9.9 d
0.2% CHX	3.3 ± 0.6 C	0.30 ± 0.03	35 ± 6.5 C	2.4 ± 0.09°	0.7 ^{E}	0.13	170 000 cm^2 p < 0.001	29.4 ± 7.2 E	70.6 ± 7.6 e

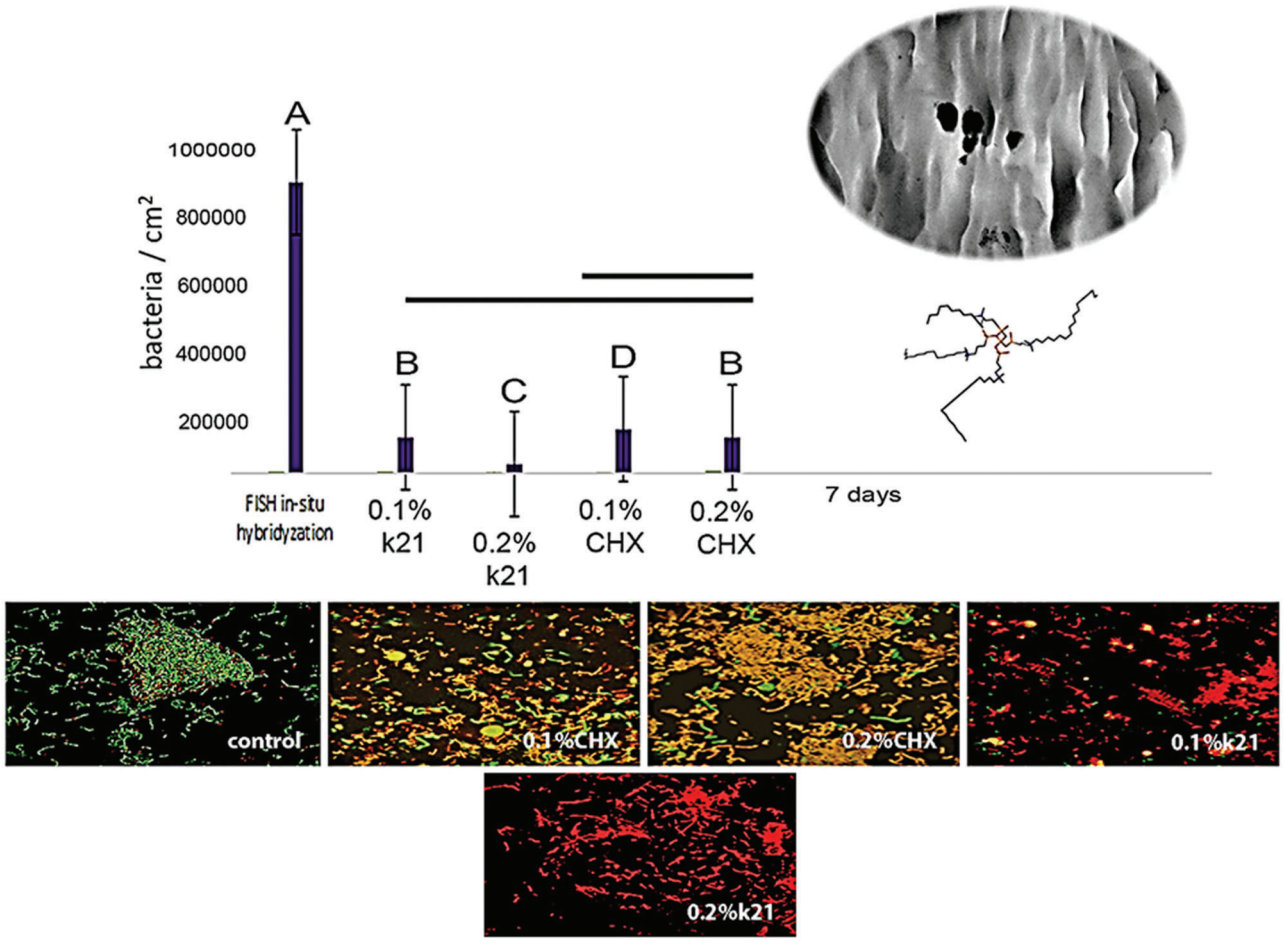

Figure 5. Quantification of A.a bacterial colonies found on collagen scaffolds after exposure was performed for seven days; $n = 3$. Cross bar represents similarity amongst groups including control (0.1% k21/0.2% CHX). CLSM images of representative groups.

Table 2. Typical band assignments of Raman spectrum of for histidine, hydroxyproline, amide I, and tryptophan. Also depicted are the percentage of crosslinking degree of different groups.

Groups	R/Histidine [cm^{-1}]	R Hydroxyproline [cm^{-1}]	R/Amide I [cm^{-1}]	R/Tryptophan [cm^{-1}]	% CX Dg	Glycine	Proline
Control	982 ± 5.7	855 ± 2.3	1655 ± 11.1	111 ± 2.1	77% ± 14.1	29.7 ± 1.9	13.1 ± 0.3
0.1% k21	984 ± 6.6	855 ± 3.1	1657 ± 5.5	113 ± 7.7	76% ± 11.1	31 ± 3.3	11.8 ± 2.1
0.2% k21	983 ± 7.1	857 ± 9.1	1660 ± 3.1	115 ± 8.1	80% ± 12.3	27.4 ± 3.9	14.4 ± 2.2
0.1% CHX	981 ± 5.6	853 ± 6.1	1651 ± 3.1	109 ± 3.1	70% ± 11.6	19.4 ± 4.1	16 ± 3.1
0.2% CHX	980 ± 8.9	852 ± 7.7	1650 ± 7.4	110 ± 9.1	79% ± 9.9	28.4 ± 3.3	12.2 ± 1.6

changes in the ultimate strain (mm/mm). The structures were difficult to handle after 5 days with multiple breaking prior to mechanical testing (data not shown).

In addition, the Table 1 shows Hz ($E'_{1\,Hz}$ and tan $(\delta)_{1\,Hz}$ values for a comparison of the mechanical properties of the different scaffolds tested. The results depicted scaffolds with more rigid structure (larger $E'_{1\,Hz}$ and smaller tan $(\delta)_{1\,Hz}$) displayed smaller strain.

The CA of the control samples was measured to 10 ± 1.22° while the experimental k21 groups measured were 0° indicating the surfaces of experimental groups highly hydrophilic with improved wettability (Table 1). Fluorescence in situ hybridization for antimicrobial analysis showed significant differences in the antimicrobial colonies between all groups with k21 groups showing the least bacterial growth ($p < 0.05$) after 7 days (**Figure 5**).

A summary of the main peaks of histidine, amides, tryptophan, and hydroxyproline with their main wavenumber shifts and band assignments are summarized in **Table 2** and **Figure 6**. The Raman spectrum was expected to dominate with organic bands with higher intensities for k21 scaffolds, confirming pro-

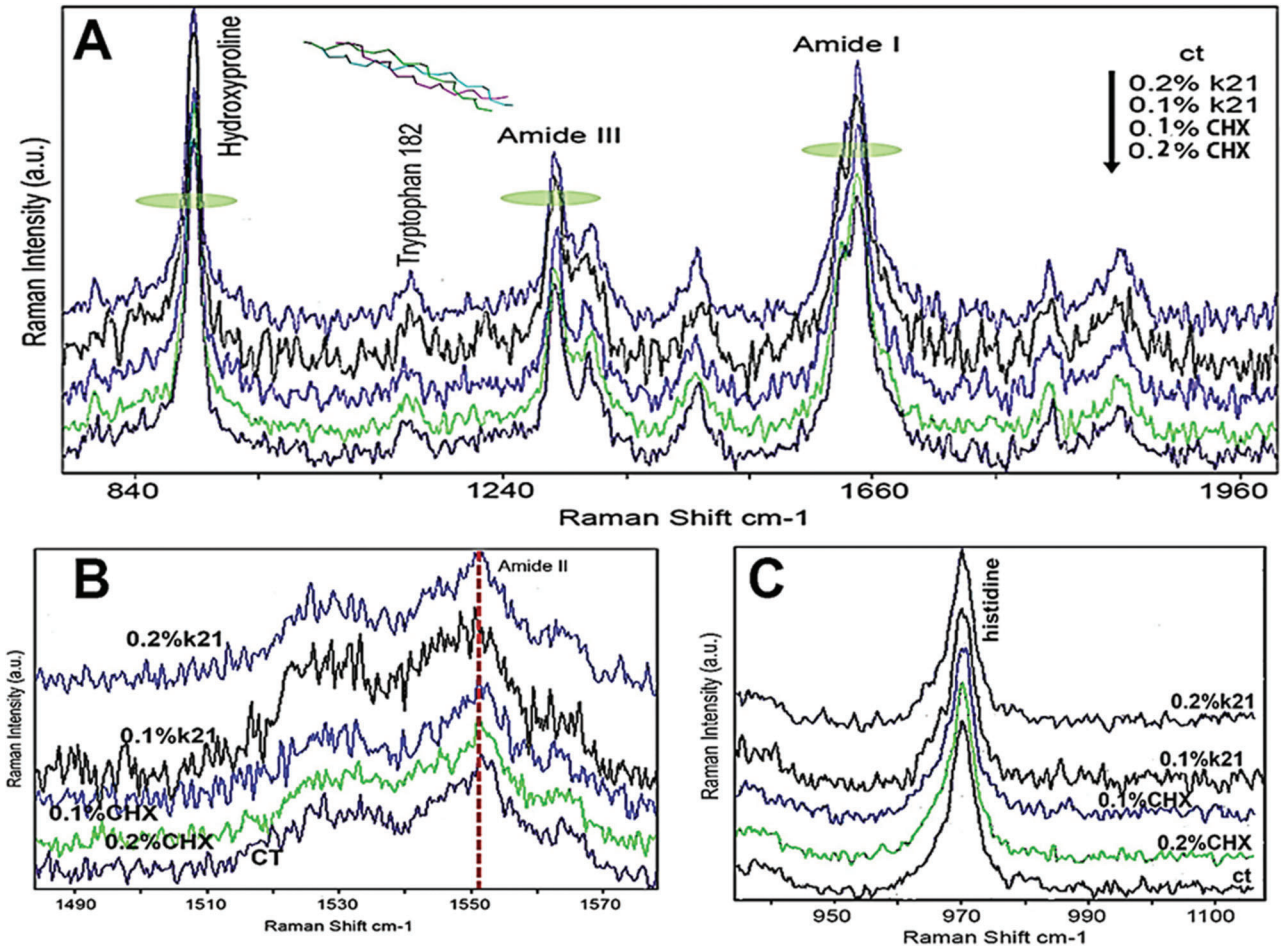

Figure 6. Raman spectra of 3D-collagen scaffold compared with the spectra of scaffold without antimicrobial or collagen crosslinking (control). The wavenumbers of the A,B) amides, tryptophan, and histidine are plotted as a function of the absolute value. All visible vibrational modes are available. A) The Raman spectra of Trp182 is excited at excited at 111 cm^{-1}. The spectra are extracted from the original spectrum. The peaks at 855, 1665, and 1246 cm^{-1} are associated with organic components for collagen. C) Raman spectra of histidine from the scaffold representing all groups (all groups followed form the arrow presented in (inset) in figure A).

tein like features (Figure 6A). The collagen is easily distinguishable from the sharp peaks seen for histidine, amides, tryptophan, and hydroxyproline (Figure 6A). However, there was no evidence of the tyrosine peaks. The baseline corrected strong hydroxyproline (855 cm^{-1}) showed a visible clear trend with highest intensities found amongst control (↔) and k21 scaffolds (right shift → k21) compared to CHX scaffolds (left shift ←), although hydroxyproline is a relatively weak Raman scatterer. Clear differences between the experimental groups were observed for the tryptophan and histidine (Figure 6C) bands ($p < 0.05$), all of which were more pronounced in the k21 groups apart from the control. The Raman analysis was furthered by using Amide I (C═O stretch) and III profiles which is considered a signature of the peptide carbonyl vibration to understand the dynamic excursions of the polypeptide backbone (Figure 6A). The modifications induced by crosslinking at the level of collagen vibrations indicate protein conformational changes. Some variability could be observed within each condition for the Amide I (1650–1690 cm^{-1}) and III bands (1256 cm^{-1}). The mean width calculated for amide and hydroxyproline/tryptophan peaks were 24 ± 13 cm^{-1}. In addition, the result was further corroborated with the emergence of well-formed Amide II (N–H in-plane bend and the C–H stretch) peak at the region of 1555 cm^{-1} (Figure 6B), with peaks dominating for k21 groups.

Additional fragmentation experiments were performed using tandom mass spectrometry spectra (m/z) resulting from CID fragmentation of the collagen protein confirming hydroxyproline (**Figure 7**). High resolution mass spectroscopy allowed differentiation of components with high confidence. Fragmentation species of hydroxyproline and proline were indicated by using COLTIA1 protein band for MALDI-MS tryptic peptides with different ion modes. Using high-resolution spectroscopy, Pro221→Hyp221 fragment was confirmed at residue 212.10, 269.12 by the presence of a b7 ion suggestive of a correct assignment. All hydroxyproline and proline residues were depicted using Swiss Plot database searching present in COLIIA1.

To better characterize the organic collagen phase of the scaffold with k21 and CHX modifications, ^{1}H MAS NMR experiments were performed with dipolar filtering (**Figure 8**A). Signals with weak H–H (isolated H atoms) were added. A strong signal

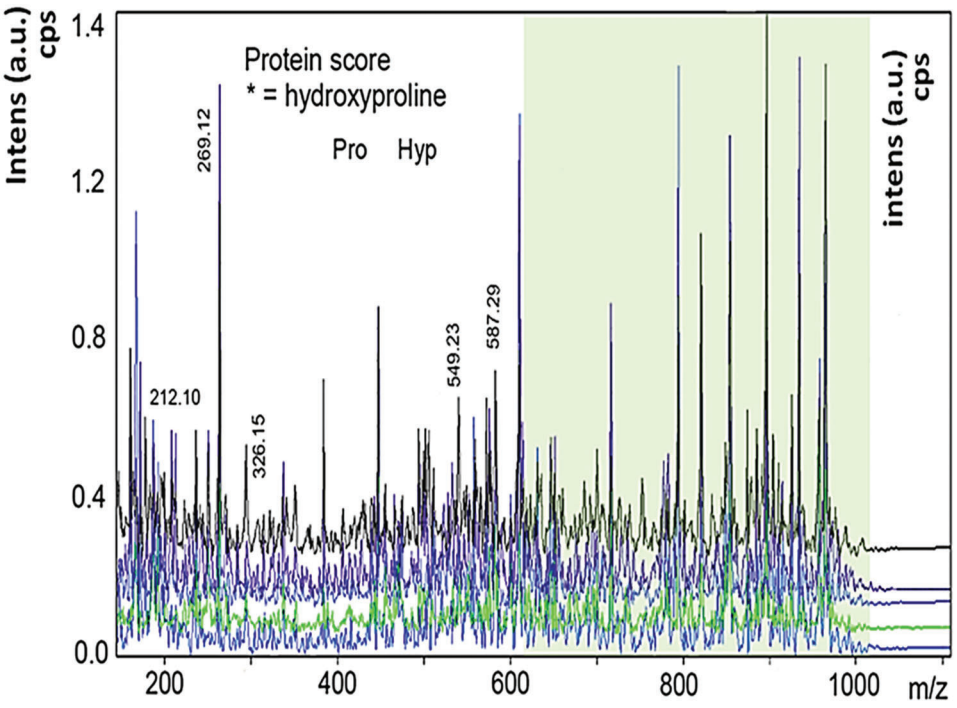

Figure 7. Tandom Mass spectrometry spectra (m/z) resulting from CID fragmentation of the collagen protein confirming hydroxyproline. High resolution mass spectroscopy allows differentiation of components with high confidence. COLTIA1 protein band used for MALDI-MS tryptic peptides showing different ion modes indicating fragmentation species of hydroxyproline and proline.

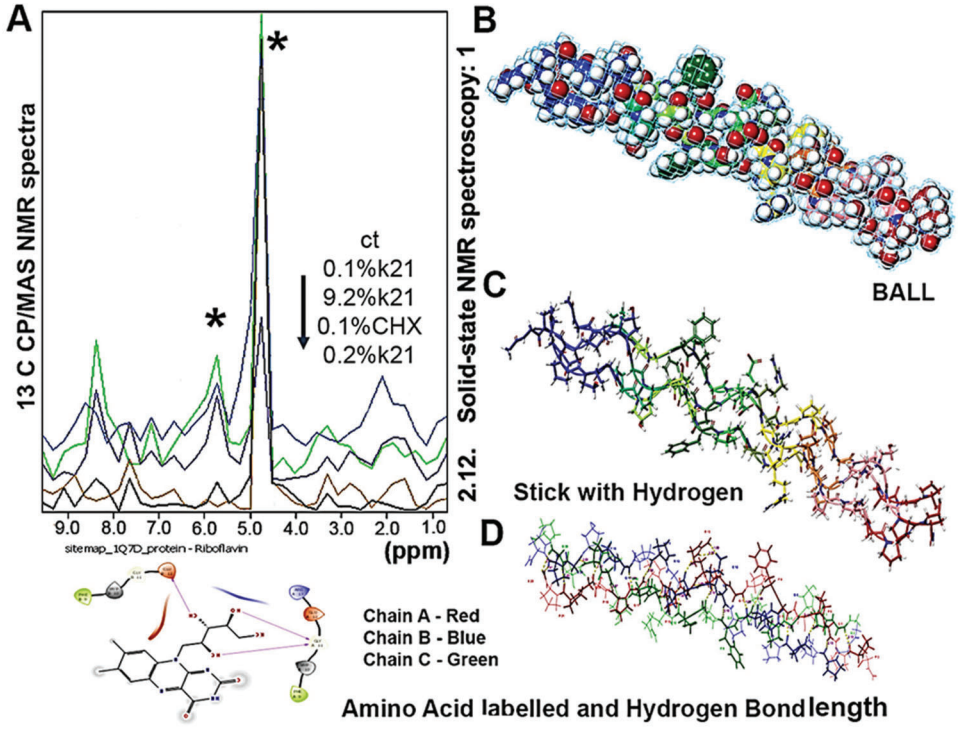

Figure 8. A) ^{13}C CP/MAS NMR spectra of printed scaffolds with different degree of deacetylation for the collagen resonance assignments and signal numbering. B–D) The crystal structure of the HPX collagen domain color balls are labeled on the homology model using the nomenclature of protease substrates relative to the scissile bond after collagen crosslinking. The triple helix structure of collagen shows surface hydrophobicity and electrostatic interaction with the D) hydrogen bonds network and covalent bonds. C) The collagen triple helix is amino acid labeled with D) hydrogen bond length. (Inset RF structure).

in the range of 4.6 to 4.8 ppm is considered as a broad superimposition of water molecule pool moderately bound to collagen helical structure in the organic phase. This effect is visible due to the dynamic behavior of amide groups confirmed also through Raman analysis. The collagen signal in the ^{1} H MAS NMR spectra were much broadened with chemical shifts within different experimental groups as k21 groups showed higher intensities. According to the results, the ratio between the OH– in scaffold and organic protons of collagen (^{1}HOH/^{1}HORG) has been calculated.

The crystal structure of the HPX collagen domain (color balls) are labeled on the homology model using the nomenclature of protease substrates (Figure 8B) relative to the scissile bond after collagen crosslinking inside the Schrodinger software. The triple helix structure of collagen shows surface hydrophobicity and electrostatic interaction with hydrogen bonds network and covalent bonds. Confirming with molecular docking to investigate the impact of collagen crosslinking on the collagen molecule packing within the fibril, the structure was modified using lysine and arginine side chain substituted between two polypeptide chains. After completing the equilibrium simulation steps, each system was simulated for 20 ns displaying multiple charged residues within the triple helix of hCOL3A1 Gly489-Gly510 after stabilization with an effective RF crosslinker. The hydrogen bonds were considered strong with flexible triple helix bending including amino acid and peptide-membrane interaction (Figure 8C). The interchain and interhelical bonds stabilized the helical structure stacking numerous hydrogen bonds with exhibited angles of 174.88°. The docked k21 molecule showed an effective binding (data not shown) with RF binding with Gly120 amino acid residue (0.252 nm) stabilizing the collagen molecule within the fibril (**Table 3**).

Table 3. Identification of hydrogen bond interaction with molecular docking.

No.	Hydrogen bond interaction between chains	Hydrogen bond length
1	X23 (A)–p21 (B)	1.97
2	X23 (A)–G20 (C)	2.62
3	P21 (A)–G20 (C)	1.93
4	G20 (B)–P18 (C)	2.0
5	P18 (A)–G17 (C)	2.07
6	G17 (A)–P15 (C)	1.94
7	G17 (A)–P15 (B)	2.0
8	P15 (A)–G14 (C)	2.01
9	R13 (B)–E12 (C)	1.96
10	R13 (B)–R13 (A)	2.24
11	R13 (A)–E12 (B)	1.89
12	R13 (A)–E12 (B)	2.79
13	E12 (A)–E12 (B)	1.96
14	E12 (A)–G11 (C)	2.16
15	G11 (B)–G8 (C)	2.16
16	G11 (A)–F9 (B)	1.93
17	P6 (C)–F9 (B)	2.13
18	G8 (A)–P6 (B)	2.05
19	P6 (A)–G5 (C)	2.10
20	P3 (B)–G5 (A)	2.13
21	P3 (A)–G2 (C)	2.13
22	F9 (A)–F9 (C)	1.96
23	P6 (B)–P3 (C)	2.20
24	G20 (A)–P18 (B)	2.12

The cross-linking degree percentages for scaffold samples are displayed in Table 2. The highest percentage of crosslinking degree were found in 0.2% CHX/79% ± 9.9 and 0.2% k21/80% ± 12.3 specimens. All specimens exhibited similar percentages of free amino groups suggestive of a high crosslinking degree when crosslinked with RF. The collagen scaffolds had the same amino acid composition with the glycine and proline content close to the expected collagen content. As observed in Table 2, the collagen expressed two hydrophilic amino acids constituting ≈35% of the amino acids found.

All the specimens produced characteristic CD spectra measured in physiological buffer exhibiting ellipticity transitions (**Figure 9**). The maximum rotary was considered between 221.5 to 197 nm minimum with a cross over point considered to 215 nm. Collagen was considered as a positive peak for the control specimens indicating a complete stability of collagen structure. The arrows within the figure are an indicated change of self-assembly amongst different groups. The positive and negative peak for the k21 groups ≈221 and 2000 nm respectively suggested the retention of triple helical structure. The peak patterns for both groups appeared similar as the peaks appeared significantly higher than the CHX scaffold groups. Analysis of the temperature decrease confirmed the consistency of the experiment.

3D-scaffolds containing 1:3 $CaCl_2$ in k21 formulations displayed XRD patterns with diffraction peaks of $CaCl_2$ appearing at d = 5.97, 3.03, 2.78, 2.1, and 2.90 A° (Figure 9B). The diffraction peaks of control and CHX modified scaffolds were found to shift to lower 2θ. This is indicative of absence of $CaCl_2$ present within the scaffold. The $CaCl_2$ was observed for all normalized peaks within the k21 scaffolds with no overlaps. Apart from the diffraction peaks found for k21 scaffolds, there is no notable peak broadening for remaining specimens.

The visualization of bacteria with confocal laser microscopy (CLSM) after fluorescence in situ hybridization (FISH) was performed with sectioning done at 0.97 µm and merged using Zeiss software. With FISH, all stained bacteria were identified as A.a with a significant impact on adhering bacteria using k21 (0.1% k21 140 000 cm^2 < 0.2% 60 000 cm^2) (Figure 4) scaffolds (p < 0.001). The number of microorganisms appeared dead (Table 1) with exposure of 0.2% k21 scaffolds (5G) compared to CHX (5F) printed scaffolds (0.1% CHX 190 000 cm^2 < 0.2% k21 170 000 cm^2).

4. Discussion

The 3D-printed collagen scaffold was obtained by supramolecular self-assembly to form a fibrous structure based on hydrophilic and hydrophobic effects. The quality of the isolated collagen was verified by TEM observations revealing interconnected fibrous network structure similar to a native extracellular matrix with a probable β-sheet structure and with amide containing chemical shifts demonstrated successfully with Raman studies. We had

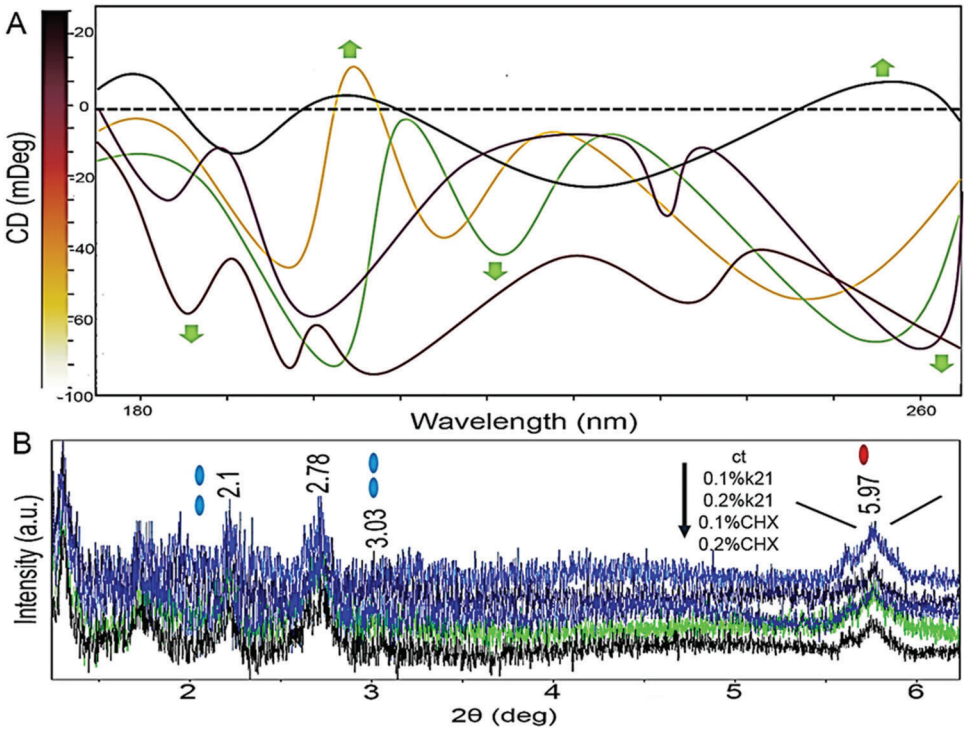

Figure 9. A) Circular dichroism spectroscopy of collagen scaffold was measured in physiological buffer exhibiting ellipticity transitions. The maximum rotary was considered between 221.5 to 197 nm minimum with a cross over point considered to 215 nm. Collagen was considered as a positive peak for the control specimens indicating a complete stability of collagen structure. The arrows are an indicated change of self-assembly amongst different groups. (ct-control; CHX-chlorhexidine) B) The XRD patterns of scaffold specimens determining the $CaCl_2$ content.

previously hypothesized that the collagen medium coupled with antimicrobial agent will not enable 3D printing of a well-defined and predictable features. With our formulations, the pressure is high enough to yield the facilitated flow continuously through the translating needle while supporting the printed features rejecting the hypothesis. However, given the lack of interface between the collagen and antimicrobial agent, it is natural to expect the mixing of both the materials. The collagen fibers appeared single and individual with no breaking of intermolecular interactions with stabilized chains and structural stability (Figure 3). Inspired by the native bone matrix, which comprises of the mineral phase embedded into a mainly collagenous network, the k21 formulation was incorporated with in order to improve a probable osteogenic potential of the designed heterophasic construct. Unsurprisingly, the type of antimicrobial used appeared to have its effect on the collagen fiber distribution. Concentrations of CHX used appeared to mask the underlying collagenous structure distancing and thinning the collagen fibers because the collagenous bundles were not visible using the TEM, as compared to the evenly distributed collagen scaffold in the case of k21 addition. The authors speculate that the highly cationic nature of CHX at the specific concentration might have a general inhibitory effect on the collagen layering. As crosslinking is a common method to stabilize collagen, both in tissues[38] and scaffolds, the 3D printed collagen scaffold was crosslinked using RF-VETPGS formulations with dental curing light. The use of blue light is a common approach[37] because it has been shown to possess the energy required to crosslink the collagen structure. Furthermore, collagen is more hydrophilic[38] which may play a role in CHX dispersion and non-attachment on the collagen scaffold.

The mechanical properties of the scaffolds were characterized by using Atomic Force Microscopy. The elastic modulus was determined using a zero deflection in the non-contact part of a force curve. It is noteworthy that a load displacement curve of the cantilever was used for indenting the scaffold producing average elastic modulus in a predictable range. The test developed in this work showed a reliable result for characterizing the mechanical properties of the scaffolds. The elastic modulus for k21 modified scaffolds showed significantly similar ($p < 0.05$) values suggesting the same stiffness and no decrease in mechanical properties after addition of the antimicrobial and crosslinking effect; an indirect evaluation of RF crosslinking effect.[33] The excessive crosslinking and presence of CHX may have altered configuration sites with less covalent sites hydrolyzing specific peptide bonds.[40] Collagen protein tends to reduce efficacy of CHX[41] as these mitigating factors might affect the CHX effect within the scaffold matrix, mainly the time of contact of this substance is short. It is observed that the k21 scaffolds had improved mechanical properties due to its stiffer nature and relationship between elastic modulus and material density.[42] Although the mechanical properties and ultimate strain showed significant improvements within the k21 scaffolds, they did not achieve a modulus close to cancellous or cortical bone (0.1–2 GPa, 15–20 GPa).[43] The ultimate strain results reveal these 3D prints can be readily compressed and inserted into defects achieving a close conformal contact. The design of the collagen scaffolds and

antimicrobial/crosslinking reinforcement is therefore tuned to improve surgical practicality and cell activity, due to the reasonable porosity measurements. These porous scaffolds are tuned to enhance cell proliferation and remodeling leading to matrix biosynthesis.[44] In addition, Table 2 shows the tangent at 1 Hz ($E'_{1\,Hz}$ and tan $(\delta)_{1\,Hz}$, for a better comparison of the mechanical properties. The more rigid scaffolds, (larger $E'_{1\,Hz}$ and smaller tan $(\delta)_{1\,Hz}$), the structures are considered less deformable, an increased in strain with the addition of crosslinker.

The change in mechanical properties and collagen arrangement specifically within the k21 scaffolds may owe to the crosslinking formulation applied. The formulation had been defined and modified from previous protocols of corneal collagen[33] and dentin collagen[27] crosslinking combining d-Alpha-tocopheryl-poly(ethylene-glycol), as a crosslinking enhancer with UVA-activated RF. Activated by ultraviolet A, the collagen cross-linker RF, known as vitamin B2-is a successful ophthalmic cross-linker used over years to reinforce the cornea and treat keratoconus. RF can create radicals ($^1O2$), and collagen crosslinking is done by forming covalent intermolecular crosslinks by photo-oxidation.[45,46] Chemical vehicles such as d-alpha-tocopherylpolyethylene-glycol 1000 succinate (D-Alpha), and ethylene-diamine tetraacetic acid have been studied in an attempt to improve RF collagen crosslinker penetration. The use of such chemical agents may allow cross-linking agents to penetrate deeper into the collagen fibrillar network.[47] The improvement in mechanical stability of 3D-printed scaffolds with RF/VE-TPGS should be considered as a further confirmation of such a synergetic effect of both the crosslinkers. The crosslinking effect help in aligning the collagen fibers more and may also help in improving the remineralization potential.[27] If this explanation of the crosslinking effect is deemed correct, changes of amino acid chains along polypeptide chains would manifest itself seen within the Raman spectra due to the crosslinking. The oscillatory mean Amide changes show a difference which is apparent between the modified scaffolds and the control groups. This is a clear indication of the collagen alignment being different within the control specimens as compared to the modified groups, giving Amide bands at a higher wavenumber position than α-helices in fibrous proteins. Despite all peaks, the hydroxyproline, tryptophan and histidine peaks are visible. For tryptophan and histidine, different concentrations of modifications induced shifts of the intensity ratios for some bands with stretching moving away from 982 cm^{-1} of the control specimen. Considering the experiments were performed at relatively high collagen concentration, it is not surprising that the tryptophan, and histidine spectra vary for the relatively small changes within different groups. The hydrogen bonding pattern of Amide groups within the collagen structure is suggestive of the Amide groups supporting the assumption that the matrix is forming an altered, more aligned, extracellular matrix to support mineralization with cross-linking in presence of k21 molecule, the antimicrobial, and $CaCl_2$ as suggestive of the XRD results. The diffraction peaks of $CaCl_2$ due to the presence of the compound with k21 could increase the mineralization potential of the scaffold which can be a double-edged sword as on one side, the presence of $CaCl_2$ can help in bone/dental tissue regeneration. These scaffolds will be of significant relevance after the incorporation of antimicrobial agents, like k21 platform chemistry, so that they can provide protection against infections after surgical implantations. The predicted protein sequence is available in the SwissProt with the presence of Hyp ensuring stabilization of triple helix structure of COLIIA1. There were planar peptide bonds within the matrix structure of the scaffolds (both k21 and CHX) after confirmation of proline and hydroxyproline presence using mass spectroscopy. This is suggestive of a triplet structure in collagen α chain space[4] with stabilization of triple helix structure.

The cytoplasmic contents of bacterial cells are perturbed and exacerbated as a result of destruction of the lipid bilayer, a signature mechanism of the QASs (k21). The QAS binds to the anionic sites found on the membrane surface causing the bacterial cells to lose their osmoregulatory capability leaking potassium ions and protons. The mode of k21 action entails the involvement of a positively charged quaternary nitrogen with phospholipid acids in the membrane. The hydrophobic tail integrates into the hydrophobic membrane core changing the membrane from fluid to liquid crystalline state with phospholipids (lipid A)[20] going into a hexagonal arrangement.[48] In the present in situ study, the number of micro-organisms decreased significantly with the exposure of k21 scaffolds ($p < 0.05$) with highest number of decrease and preferential bacterial colonization seen in 0.2% k21 scaffolds. All bacteria were identified as A.a evaluating the bacterial colonization on baseline during culture and 7 days. The pronounced variability seems to be characteristic of k21 being more effective than CHX as referenced with our previous studies.[25] A.a are regarded as the principal periodontal pathogens. The virulence factors include immunosuppressive factors, leukotoxins, and a high capacity to invade cells. There is a host response to these periodontal pathogens against infection, however, a persistence of these pathogens may render the protective roles of inflammatory cells dangerous to the host tissues.[49] The decrease in bacterial population owing to the effect of k21 modified scaffolds warrants the rejection of the second null hypothesis that the k21 content had no effect, in relevance to single species biofilms. Thus, in the current study, the results indicated the antimicrobial effectiveness of k21 bound collagen scaffolds with 0.2% as the minimal concentration to achieve the desired efficacy and hence could overcome any short comings of existing collagen-based scaffolds or membranes being belligerent against bacterial colonies. CHX is water-soluble and can leach put from surfaces resulting in loss of antimicrobial potency and has poor water solubility.[50] The sol gel method used to prepare the k21 molecule provides a facile method with tetrafunctional organosilane which pivots as an anchoring unit trialkoxysilane molecules enabling a 3D network[51] to be formed once condensation is brought to completion. Once condensed, this reduces the possibility for the SiQAC molecule to leach out of the scaffold providing considerably longer antimicrobial effect when compared to CHX. Also, a strong covalent attachment is expected due to the presence of reactive silanol groups present within the k21 molecule via Si–O linkages to exert non-migrating microbiocidal functions,[21] a surfactant activity showing notable changes in the CA measurements within the matrix printed. The addition of k21 molecule is expected to increase the overall surface energy[52] due to roughness of the scaffold as compared to CHX modification. This can alter the CA as seen in all k21 scaffold specimens, also including the 0.1% CHX specimen. The k21 scaffolds showed increased wettability and 0° CA due to the surface characteristics. The increased polar component of the

surface energy results in lower CAs with the lower CAs resulting in increased wetting.

The best fitted poses as a result of docked RF molecules are shown in Figure 8. The RF binding was effectively verified by showing electrostatic attractions present within the RF binding effectively with the nitrogen atoms of the Gly 120 amino acid residue (2.52 Å). The analysis of the sequences of the peptides provided strong evidence of these crosslinks by presentation of the triple helix structure of collagen with surface hydrophobicity and electrostatic interaction with the hydrogen bonds network and covalent bonds. There was retention of the collagen crosslink and residues involved giving the highest efficiency to induce collagen crosslinking. This collagen crosslinking is known to be mediated by $^1O_2$ via secondary reactions between nucleophilic residues (Lys, and Cys) and carbonyl groups. Comparison of the data obtained from control and crosslinked samples indicated the formation of specific crosslinks. This was also indicated in the CD spectra of the collagen which revealed peaks distinctive of peptide linkages for all the scaffolds. This was a confirmation for backbone configuration with hydroxyproline further endorsed by the results obtained with Tandom Mass spectroscopy and crosslinking degree.

Despite the aforementioned approaches to incorporate antimicrobial material component or drug compounds inside a 3D printed scaffold, this progress is limited to in vitro experiments. The knowledge gap or lack of complete understanding is the basic biological status and seeding of human pulpal dental stem cells or periodontal stem cells for optimized tissue regeneration. All factors that determine and provide periodontal tissue formation have not been clarified in this project. Further studies are warranted to quantify the crosstalk between periodontal stem cell populations across the scaffold and evaluate its potential on cell migration. Moreover, an in-depth understanding of the basic biology is indispensable to provide more detailed information to guide the fabrication of a suitable biomimetic material-based scaffold. The goal of this project was to develop a 3D printed collagen-based crosslinked scaffold with engineered microstructural properties for future use in the development of stratified tissues. The antimicrobial crosslinked collagen scaffold can now be engineered and fine tuning to control several properties like degradation profiles, swelling, and transport across the network is valuable work for the future.

5. Conclusion

Using 3D printing of collagen scaffolding, this was a successful production of collagen scaffold with a potent antimicrobial and crosslinked stability. The matrix features were somewhat similar to those in tissues of collagen matrices with antimicrobial capacity.

Supporting Information

Supporting Information is available from the Wiley Online Library or from the author.

Acknowledgements

The authors thank the laboratories at School of Dentistry International Medical University Kuala Lumpur and Faculty of Dentistry National University of Singapore, Centre of Bioactive Molecules & Drug Delivery, Institute for Research, Development & Innovation International Medical University, Kuala Lumpur, and Mimos Research Center Malaysia for the research experiments and analysis. This work was supported by International Medical University grant 505/2020 and FRGS/1/2020/SKK0/IMU/02/10 project. The study was also supported by KHG fiteBac Technology, Marietta, GA, USA. The k21-E Irrigant used in this study was supplied by KHG fiteBac Technology, Marietta, GA, USA.

Conflict of Interest

The authors declare no conflict of interest.

Data Availability Statement

The data that support the findings of this study are available on request from the corresponding author. The data are not publicly available due to privacy or ethical restrictions.

Keywords

3D printing, antimicrobial, collagen scaffold, membranes, quaternary ammonium silane

Received: August 14, 2021
Revised: November 26, 2021
Published online:

[1] C. I. L. Chapple, *J. Dent.* **1997**, *25*, 3.
[2] G. N. R. B. Chandra, K. L. Vandana, *CODS J. Dent.* **2017**, *9*, 22.
[3] K. G. Murphy, J. C. Gunsolley, *Ann. Periodontol.* **2003**, *8*, 266.
[4] S. Nyman, *J. Clin. Periodontol.* **1991**, *18*, 494.
[5] T. Karring, S. Nyman, J. Gottlow, L. Laurell, *Periodontol. 2000* **1993**, *1*, 26.
[6] J. Majzoub, S. Barootchi, L. Tavelli, C.-W. Wang, S. Travan, H.-L. Wang, *J. Periodontol.* **2020**, *91*, 1148.
[7] D. S. Sari, E. Maduratna, F. D. E. Latief, A. P. Nugraha, K. Sudiana, F. A. Rantam, *Eur. J. Dent.* **2019**, *13*, 206.
[8] W. Zheng, S. Wang, J. Wang, F. Jin, *Int. J. Mol. Med.* **2013**, *36*, 915.
[9] C. Soo, G. Rahbar, R. L. Moy, *J. Dermatol. Surg. Oncol.* **1993**, *19*, 431.
[10] S. Pitaru, H. Tal, M. Soldinger, M. Noff, *J. Periodontal. Res.* **1989**, *24*, 247.
[11] A. D. Nocera, R. Comín, N. A. Salvatierra, M. P. Cid, *Biomed. Microdevices* **2018**, *20*, 26.[CrossRef]
[12] A. Sculean, A. Stavropoulos, P. Windisch, T. Keglevich, T. Karring, I. Gera, *Clin. Oral Invest.* **2004**, *8*, 70.
[13] R. Parodi, G. Carusi, G. Santarelli, F. Nanni, R. Pingitore, G. Brunel, *Int. J. Periodontics Restorative Dent.* **1997**, *3*, 282.
[14] C. Stoecklin-Wasmer, A. W. S. Rutjes, B. R. Da Costa, G. E. Salvi, P. Jüni, A. Sculean, *J. Dent. Res.* **2013**, *92*, 773.
[15] J. Rouwkema, S. Gibbs, M. P. Lutolf, I. Martin, G. Vunjak-Novakovic, J. Malda, *J. Tissue Eng. Regener. Med.* **2011**, *5*, e164.
[16] S. Vanaei, M. S. Parizi, S. Vanaei, F. Salemizadehparizi, H. R. Vanaei, *Eng. Regener.* **2021**, *2*, 1.
[17] D. Devore, J. Zhu, R. Brooks, R. R. Mccrate, D. A. Grant, S. A. Grant, *J. Biomed. Mater. Res., Part A* **2016**, *104*, 758.
[18] L. Anil, V. Kl, *Int. J. Mol. Biol.* **2021**, *3*, 73.
[19] U. Daood, A. Parolia, J. Matinlinna, C. Yiu, H. M. A. Ahmed, A. Fawzy, *Dent. Mater.* **2020**, *36*, e386.
[20] U. Daood, J. P. Matinlinna, M. R. Pichika, K.-K. Mak, V. Nagendrababu, A. S. Fawzy, *Sci. Rep.* **2020**, *10*, 10970.

[21] U. Daood, C. Yiu, M. F. Burrow, L.-N. Niu, F. R. Tay, *J. Dent.* **2017**, *60*, 77.
[22] U. Daood, C. Yiu, M. F. Burrow, L.-N. Niu, F. R. Tay, *J. Dent.* **2017**, *58*, 19.
[23] B. Ahlström, R. A. Thompson, L. Edebo, *APMIS* **1999**, *107*, 318.
[24] A. J. Isquith, E. A. Abbott, P. A. Walters, *Appl. Microbiol.* **1973**, *24*, 859.
[25] U. Daood, M. F. Burrow, C. K. Y. Yiu, *Clin. Oral Invest.* **2020**, *24*, 649.
[26] N. Y. Turova, E. P. Turevskaya, V. G. Kessler, M. I. Yanovskaya, *The Chemistry of Metal Alkoxides*, Kluwer Academic Press, Norwell **2020**.
[27] A. E. Danks, S. R. Hall, Z. Schnepp, *Mater. Horiz.* **2016**, *1*, 91.
[28] M. Tischer, G. Pradel, K. Ohlsen, U. Holzgrabe, *Chem. Med. Chem.* **2012**, *7*, 22.
[29] O. Moses, D. Vitrial, G. Aboodi, A. Sculean, H. Tal, A. Kozlovsky, Z. Artzi, M. Weinreb, C. E. Nemcovsky, *J. Periodontol.* **2008**, *79*, 905.
[30] A. K. B. Bedran-Russo, P. N. R. Pereira, W. R. Duarte, J. L. Drummond, M. Yamauchi, *J. Biomed. Mater. Res., Part B* **2007**, *80B*, 268.
[31] U. Daood, K. Iqbal, L. I. Nitisusanta, A. S. Fawzy, *J. Biomed. Mater. Res.* **2013**, *101A*, 1846.
[32] a) A. S. Fawzy, L. I. Nitisusanta, K. Iqbal, U. Daood, J. Neo, *Dent. Mater.* **2012**, *28*, 1284. b) C.-F. Cheng, K.-M. Wu, Y.-T. Chen, S.-L. Hung, *J. Formosan Med. Assoc.* **2015**, *114*, 35.
[33] U. Daood, J. P. Matinlinna, A. S. Fawzy, *Dent. Mater.* **2019**, *35*, 356.
[34] S. Hayes, C. S. Kamma-Lorger, C. Boote, R. D. Young, A. J. Quantock, A. Rost, Y. Khatib, J. Harris, N. Yagi, N. Terrill, K. M. Meek, *PLoS One* **2013**, *8*, e52860.
[35] A. Leccisotti, T. Islam, *J. Refractive Surg.* **2010**, *26*, 942.
[36] A. Stojanovic, W. Zhou, T. P. Utheim, *Biomed. Res.* **2014**, *2014*, 1.
[37] C. Caruso, C. Ostacolo, R. L. Epstein, G. Barbaro, S. Troisi, D. Capobianco, *Cornea* **2016**, *35*, 145.
[38] G. Wollensak, H. Aurich, C. Wirbelauer, D.-T. Pham, *Ophthalmic Res.* **2009**, *41*, 114.
[39] S. Muthusamy, S. Kannan, M. Lee, V. Sanjairaj, W. F. Lu, J. Y. H. Fuh, G. Sriram, T. Cao, *Biotechnol. Bioeng.* **2021**, *118*, 3150.
[40] R. Seseogullari-Dirihan, L. Tjäderhane, D. H. Pashley, A. Tezvergil-Mutluay, *Dent. Mater.* **2015**, *31*, 1225.
[41] B J. Rasimick, J. Wan, B. L. Musikant, A. S. Deutsch, *J. Endod.* **2010**, *36*, 489.
[42] M. L. A. Gibson, B. Harley, *Cellular Materials in Nature and Medicine*, 1st ed., Cambridge University Press, Cambridge **2010**.
[43] R. G. Pearson, R. Bhandari, R. A. Quirk, K. M. Shakesheff, *Trends Biotechnol.* **2012**, *27*, 199.
[44] B. Harley, J. Leung, E. Silva, L. Gibson, *Acta Biomater.* **2007**, *3*, 463.
[45] G. R. Snibson, *Clin. Exp. Ophthalmol.* **2010**, *38*, 141.
[46] G. Wollensak, E. Spoerl, T. Seiler, *Am. J. Ophthalmol.* **2003**, *135*, 620.
[47] C. Ostacolo, C. Caruso, D. Tronino, S. Troisi, S. Laneri, L. Pacente, A. Del Prete, A. Sacchi, *Int. J. Pharm.* **2013**, *440*, 148.
[48] P. Gilbert, L. E. Moore, *J Appl. Microbiol.* **2005**, *99*, 703.
[49] B. Henderson, S. P. Nair, J. M. Ward, M. Wilson, *Annu. Rev. Microbiol.* **2003**, *57*, 29.
[50] D. M. Foulkes, *J. Periodontal Res., Suppl.* **1973**, *8*, 55.
[51] Y. Liu, D. Xu, Y. Wu, H. Sun, H. Gao, *J. Non-Cryst. Solids* **2004**, *4*, 61.
[52] C. Grant, B. Erick, A. Preston, W. James, *Prog. Org. Coat.* **2016**, *3*, 91.

